Preprint typeset in JINST style - HYPER VERSION

Construction and test of a 1x1 m^2 Micromegas chamber for sampling hadron calorimetry at future lepton colliders

A. Author[a], B. Author[b*] and C. Author[b]

[a] *Name of Institute,*
Address, Country
[b] *Name of Institute,*
Address, Country
E-mail: `CorrespondingAuthor@email.com`

ABSTRACT: Gaseous sampling hadron calorimeters can be finely segmented and used to record showers with high spatial resolution. This imaging power can be exploited at a future linear collider experiment where the measurement of jets by a Particle Flow method will rely first on the tracking capability of the calorimeters. As a result of the relaxed constrain on energy resolution, a hadron calorimeter equipped with granular gaseous detectors read out by simple threshold electronics is considered. For this application, Micromegas chambers of a few meter square size offer some advantages over traditional gaseous detectors using wires or resistive plates. To test the validity of this concept, a Micromegas prototype of $1 \times 1\,\mathrm{m}^2$ size equipped with 9216 pads of $1 \times 1\,\mathrm{cm}^2$ has been built. Its technical and basic operational characteristics are reported.

KEYWORDS: Keyword1; Keyword2; Keyword3.

*Corresponding author.

Contents

1. Introduction

1.1 Particle Flow calorimetry

The detailed study of electroweak symmetry breaking and of the properties of a hypothetical standard model Higgs boson are some of the physics goals motivating the construction of a linear electron collider (ILC [1] or CLIC [2]). The physics case is now enhanced with the discovery at LHC of a Higgs-like new particle [3]. Most of the interesting physics channels at a linear collider will appear in multi-jet final states, often accompanied by charged leptons and missing transverse energy. The di-jet energy resolution should be good enough to identify Z and W bosons in their hadronic decay channels with an accuracy comparable to their natural decay width. This requires an excellent jet energy resolution of 3–4 % over the whole energy range.

Two techniques are studied by the DREAM [4] and CALICE [5] collaboration to meet this goal. The first one, called Dual Readout, is a compensation technique that uses cherenkov and scintillation light produced in hadron showers to correct for fluctuations of the electromagnetic fraction which otherwise dominate the jet energy resolution [6]. The Particle Flow technique uses highly segmented calorimeters and a precise tracker to separate the jet's charged and neutrals components [7]. After separation, the dominant charged component can be measured more precisely with the tracking system resulting in improved jet energy resolution [8].

1.2 Semi-digital hadron calorimetry

Two hadron calorimeters using steel or tungsten absorbers are developed by the the CALICE collaboration. The first is instrumented with $3 \times 3\,\mathrm{cm}^2$ scintillating tiles read out by SiPM and 12-bit ADCs [9]. The second uses gaseous detectors with smaller segmentation ($1 \times 1\,\mathrm{cm}^2$) and simpler readout (1 or 2-bit). Clearly, the first favours single hadron resolution (higher sampling fraction, analogue readout) while the second targets a high shower separation capability (smaller cells) probably at the expanse of resolution (digital readout).

A digital hadron calorimeter (1-bit, DHCAL) is expected to have two regimes of operation. A low energy linear regime where the response to the electromagnetic and hadronic shower parts, taken separately, is constant. In this regime, Landau fluctuations are suppressed resulting in improved resolution with respect to a perfect analogue readout. A higher energy saturated regime where energy information is lost due to under-counting with the consequence that the resolution degrades with increasing hadron energy [**?**]. The energy frontier between the two regimes depends mainly on the cell size and absorber material. In an SiD-like HCAL geometry with $1 \times 1\,\mathrm{cm}^2$ pads and steel absorbers [12], Monte Carlo simulation indicates a frontier at 20–30 GeV.

The electromagnetic part of hadron showers results in dense energy deposits and is responsible for the saturation of a DHCAL. A way to account for these deposits in the energy reconstruction is to use additional readout thresholds (2-bit, semi-digital HCAL or SDHCAL). With a careful optimisation of the thresholds, it should be possible to correct for the saturation and improve, to some extend, the resolution.

1.3 The Micromegas detector and calorimeter project

Micromegas is a Micro Pattern Gas Detector (MPGD) that uses a thin mesh to separate the gas volume into two regions [13]. A low field region where primary electrons are released from the atoms and a high field region where they are drifted to and multiplied by avalanche. Thanks a fast collection of the avalanche ions, Micromegas is free of space charge effects up to very high particle rates and therefore well suited for tracking in high rate environments. This property also makes this detector very appealing for calorimetry because signals are proportional to the energy deposited in the drift region. This is an improvement with respect to wire chamber based gaseous calorimeters which suffered from intrinsic signal saturation from the ion space charge around the wire. Also, ageing effects in Micromegas are minimal because it works in simple gas mixtures (*e.g.* Ar/CO_2) and at relatively low electric fields ($\sim 40\,\mathrm{kV/cm}$ with a multiplication gap of $128\,\mu\mathrm{m}$).

The Micromegas calorimeter project was initiated in 2006. The first step of the project was the characterisation of small prototypes equipped with standard electronics (external front-end boards and VME ADC modules). Based on the successful results ([14]), the project moved on to the next phase, namely the integration of the electronics on the detector printed circuit board (PCB) and the scaling up of the detector size.

2. Description of the $1 \times 1\,\mathrm{m}^2$ Micromegas prototype

2.1 Active sensor units

An Active Sensor Unit (or ASU) is a $32 \times 48\,\mathrm{cm}^2$ printed circuit board (PCB of 8 layers, 1.2 mm thin) segmented into 1536 anode pads of $1 \times 1\,\mathrm{cm}^2$. It is equipped with a Micromegas mesh and 24 front-end chips. The mesh is laminated on the PCB pad plane according to the Bulk process [15]. Packaged chips are soldered to the PCB side opposite to the mesh, together with spark protection diodes, other passive components and flat connectors.

The ASU chips are read out with 2 Detector Interface boards (DIF, inter-DIF) which also distribute voltage to the front-end electronics and to the Micromegas mesh. ASU and inter-DIF are connected with flat cables in order to minimise the detector thickness and to allow for some mechanical flexibility between the 2 boards. Thanks to flat connectors on both sides of the ASU, several ASUs can be read out in a row (Figure 1 (left)). This is essential in view of the construction of large area chambers as several ASUs can be chained and read out with only one pair of DIF/inter-DIF boards.

2.2 Front-end electronics

The ILC beam will be pulsed and composed of 1 ms long bunch trains separated by 199 ms. During a train, bunches cross each other every 300 ns and calorimeter signals are digitised automatically and associated to the time of a bunch. Between trains, all information is read out from memory to the back-end electronics meanwhile some front-end circuits are turned off to reduce the heat dissipation inside the calorimeter modules. Key features of the front-end electronics are thus self-triggering with memory, time-stamping and power-pulsing.

A dedicated front-end chip called MICROROC has been developed [16]. It belongs to a generation of chips developed for the various calorimeters at a future linear collider ([17]). The MICROROC is a 64 channel chip, with 3 readout thresholds and a power-pulsing capability to reduce its consumption below a nominal value of 3.7 mW at 3.5 V per channel. Each channel input is protected against spark currents by a diode network followed by a charge preamplifier and 2 shapers of low/high gains and tunable peaking time (75–200 ns). The shaper outputs are connected to three discriminators. When a signal crosses the low threshold, the content of the 64 channel matrix is written to memory with a clock time (so-called event). A total of 127 events can be recorded before filling completely the memory. The later is read out either when it is full (ILC or trigger-less mode) or upon the arrival at the chip of an external trigger signal (testbeam mode).

The high gain shaper is connected to the low and medium threshold discriminators and has a dynamic range of 200 fC. The low gain shaper has a linear response up to 500 fC and is connected to the high threshold discriminator. The 3 thresholds are set by 10-bit DACs common to the 64 channels. Per channel, however, a 4-bit DAC can be used to shift the pedestal voltage with respect to the common thresholds and minimise their dispersions. A detailed characterisation of the detector can be performed thanks to the calibration test input and a multiplexed analogue output. Calibration of the electronics is discussed in section 3.1 and the analogue readout of Micromegas signals is explained in section 4.7.

2.3 Mechanical design

Mechanical constraints to build an ILC hadron calorimeter are stringent. First of all, the calorimeter will be located inside the solenoid magnet which limits the space between absorbers to 8 mm. Also, to minimise dead zones between modules, the font-end electronics is embedded inside the active layers and only readout boards are foreseen at the ends of the modules. Another challenge is the size of active layers which reaches up to $1 \times 3\ \mathrm{m}^2$ in the SiD design.

Modular and scalable to larger sizes, the $1 \times 1\ \mathrm{m}^2$ Micromegas prototype consists of 6 ASUs assembled in a one gas volume (Figure 1). Small spacers are inserted in the 1 mm gap between ASUs and support the cathode cover, defining precisely a drift gap of 3 mm (Figure 2). Plastic frames are closing the chamber sides, leaving openings for 2 gas pipes and flat cables for electronics connections. The chamber is eventually equipped with readout boards (3 pairs of DIF/inter-DIF) and a patch panel for voltage distribution.

The total chamber thickness amounts to roughly 9 mm which includes 2 mm for the cathode cover, 3 mm of drift gap and 4 mm for PCB and ASICs. With this mechanical design, the fraction of non-instrumented area is less than 2 % of the total area defined by the 6 ASUs. Dead zones are mainly caused by the 1 mm gap between ASUs and the 2 mm wide inactive photoresist strips that support the mesh on the four ASU sides.

3. Tests prior to chamber assembly

3.1 Electronics calibration

3.1.1 Method

The calibration enables setting the 3 thresholds by providing the electronic gain (DAC/fC) of the two shapers. It consists in injecting voltage pulses to the test capacitor of each channel and changing the relevant threshold every 100 pulses. For a given pulse height (or test charge Q), the channel response (0/1) versus threshold is measured and latter differentiated. The gain and noise of the shapers is deduced from the mean μ and root mean squared (RMS) σ of the resulting distribution. Non-linearity of the shaper response are also checked by injecting different test charges: 2.5, 12.5,

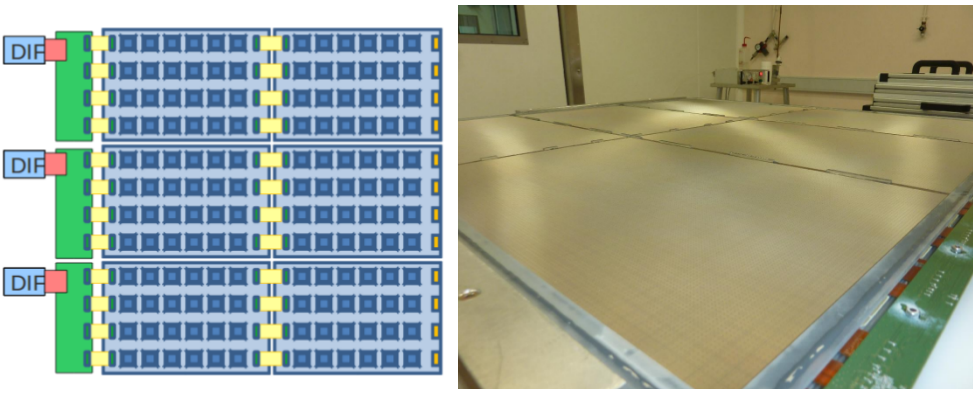

Figure 1. Drawing of the chip side of the $1 \times 1\ \mathrm{m}^2$ prototype showing the readout boards (DIF, inter-DIF), the ASUs and the flexible connectors between them (left). Photograph of the mesh side of the prototype and the drift cover during assembly (right).

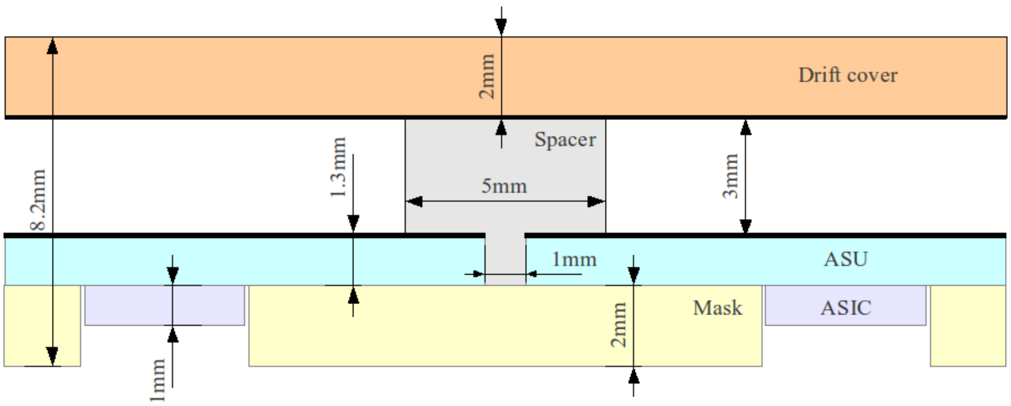

Figure 2. Mechanical design of the $1 \times 1\ \mathrm{m}^2$ prototype at a junction between 2 ASU.

22.5 and 32.5 fC for the high gain shaper and 100 and 200 fC for the low gain shaper. The electronic calibration was performed with a single chip test board after the MICROROC production and a yield of 91.5 % was found. After bounding of the chips to the PCBs and lamination of the Bulk mesh, another calibration was performed on the 6 available ASU giving compatible results. These results are presented in the following section.

3.1.2 Shaper gains and noise

The gain of the shapers of 9216 channels is distributed around a mean value of 7.1 DAC/fC (high gain) and 1.6 DAC/fC (low gain). The channel to channel variation in both cases is $\sim 3\,\%$ RMS (Figure 3 (left and centre)). This is 3 times smaller than the signal variations induced by mechanical imperfections of the Micromegas gaps which eventually dominate the response uniformity of this Micromegas detector ([14]).

The low threshold discriminator triggers the writing to memory of the 64 channel content. It is connected to the output of the high gain shaper and therefore only the noise of this shaper is relevant for our purposes. Calculating the noise as σ divided per the gain, an average noise of

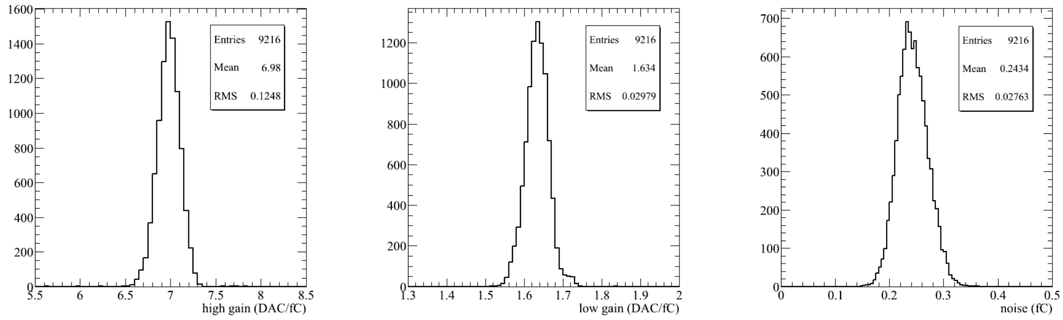

Figure 3. From left to right: gains of the 2 shapers and noise at the output of the high gain shaper for all channels of the $1 \times 1\ \mathrm{m}^2$ prototype.

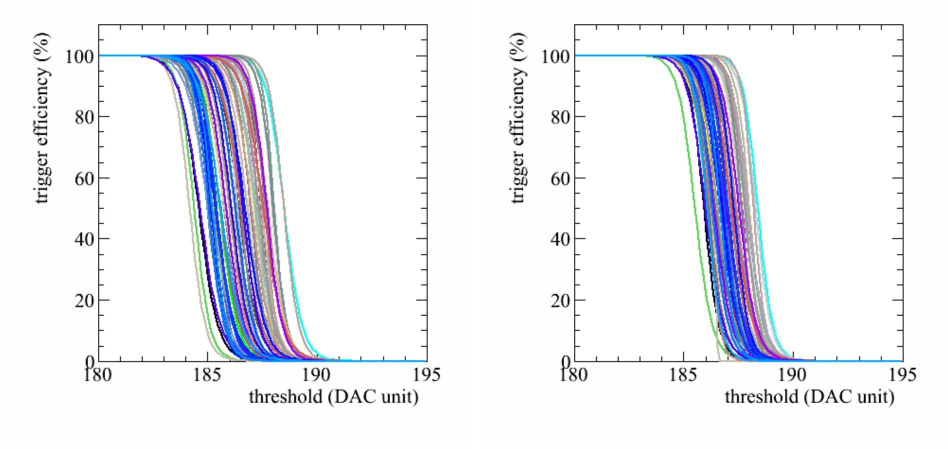

Figure 4. Pedestals of 64 channels measured in a threshold scan before and after alignment (left and right).

0.2 fC is found with 10 % variations. This is quite small compared to a typical Micromegas MIP signal of 5–10 fC and close to what was measured before bounding of the chips to the PCB. It can thus be concluded that the design of the PCB do not increase the noise level at the channel inputs.

3.1.3 Setting of thresholds and pedestals

The 3 threshold DACs of a MICROROC are common to the 64 channels. The lowest possible threshold is therefore determined by the channel of highest pedestal, for instance $5\,\sigma$ above the pedestal. Also, channels with lower pedestals will experience larger thresholds. As a result, individual channel DACs have been implemented to change the pedestals and correct the channel thresholds by a few fC. A method to align the pedestal (and thus to equalise the thresholds) is to adjust the individual DAC values so as to obtain a uniform noise rate over the all channels. It is illustrated in Figure 4 and allows to reduce the threshold spread from 4 to 2 fC RMS. This is a significant improvement because a smaller threshold spread allows a lower operating gas gain and low gain operation is always preferred.

In a semi-digital calorimeter, values of the medium and high thresholds should be optimised for best energy resolution over the relevant energy range. This optimisation is meaningful for test of a full calorimeter, not for single chamber test. During the test beam period reported in section 4, default settings of 5 and 15 MIPs have been chosen.

3.2 X-ray tests

Counting experiments are performed with an ^{55}Fe 5.9 keV X-ray source to characterise the ASUs before they are sealed in the $1 \times 1\,\mathrm{m}^2$ prototype. A dedicated gaseous chamber with 14 mm drift gap and perforated drift cover has been constructed to measure the response of any of the 1536 ASU channels to true Micromegas signals.

In a non flammable mixture of Ar/CF_4/iC_4H_{10} 95/3/2, ^{55}Fe quanta can convert in the gas mainly by photoelectric effect on an argon atom, resulting on average in 115 or 230 primary electrons depending on the involved atom relaxation processes: fluorescence (escape peak) or Auger cascade (photopeak) [18]. After drifting, mostly all primary electrons are multiplied in the amplification gap [14]. If above threshold, the pad signal is recorded as a hit in the chip memory. The counting rate was measured for various sets of experimental parameters (thresholds, mesh voltage and pad position). Each run lasted 60 s and the drift field was set to 300 V/cm which correspond to the local maximum of the drift velocity in the gas mixture used. Results are presented and discussed in the following sections.

3.2.1 Threshold scans

The gas gain curve is deduced from measurements of the counting rate R versus threshold t at various mesh voltages and inputs from the electronic calibration (shaper gains). Low threshold scans were performed at voltages between 300 and 350 V. At a drift field of 300 V/cm, the average spread of a point-like cloud of electrons (from photoelectric conversion) at the mesh is $\sim 230\,\mu$m in the direction transverse to the field and ~ 2 ns in time [19]. With the source collimated to the centre of a pad, most primary electrons are collected on one pad. For simplicity all other pads were electronically disabled. The results are shown in Figure 5. Each $R(t)$ trend is well described by the sum of two sigmoid functions accounting for the photopeak and the escape peak:

$$R(t) = \frac{p_0}{1+\exp\left(\frac{t-p_1}{p_2}\right)} + \frac{p_3}{1+\exp\left(\frac{t-p_4}{p_5}\right)} \tag{3.1}$$

where the parameters (p_0, p_3) are the rates at zero threshold, (p_1, p_4) the inflexion thresholds at the peak maxima and (p_2, p_5) are proportional to the peak widths. In order to reduce the number of parameters fitted to the data points, the following approximations between photopeak and escape peak are used:

$$\frac{p_0}{p_3} = \frac{1-f}{f} = \frac{85}{15} \tag{3.2}$$

where f is the fluorescence yield of an excited argon atom [20]. Noting E_{pp} and E_{ep} the energy of the photopeak and escape peak:

$$\frac{p_1}{p_3} = \frac{E_{\mathrm{pp}}}{E_{ep}} = 2 \tag{3.3}$$

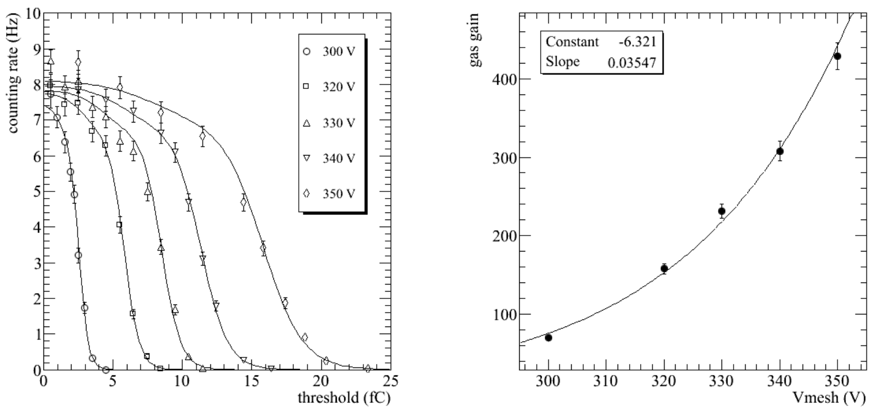

Figure 5. Counting rate versus threshold (left) and resulting gas gain curve (right).

$$\frac{p_2}{p_3} = \sqrt{\frac{E_{\mathrm{pp}}}{E_{ep}}} = \sqrt{2} \tag{3.4}$$

so Equation 3.1 becomes:

$$R(t) = p_0 \left[\frac{0.85}{1 + \exp\left(\frac{t - p_1}{p_2}\right)} + \frac{0.15}{1 + \exp\left(\frac{t - 0.5 p_1}{p_2/\sqrt{2}}\right)} \right] \tag{3.5}$$

After fitting, all hit rates converge to roughly 8 Hz at zero threshold. Taking an average of 230 primary electrons for photopeak events, the measured charge at the inflexion points (p_1) is used to calculate the gas gain. The gain exhibits the usual exponential dependence on the mesh voltage (Figure 5) with a slope of 0.032 / V typical of argon-based gas mixtures [21]. At 350 V, a scan of the high threshold was performed too. The resulting $R(t)$ trend is showed in Figure 6 together with the low threshold trend. The two threshold scans give gas gain values of 323 and 300 respectively. The agreement is reasonable and the 4 % difference can probably be explained by systematic errors during the calibration.

3.2.2 Mesh voltage scan

The smallest detectable charge can be deduced from a measurement of the counting rate versus gas gain. In this study, the source is still collimated to the centre of a single pad while the other pads are disabled. The threshold of the tested pad is set by iteratively decreasing the DAC until the count rate becomes dominated by noise. The final DAC value is then set one unit above this steep transition so this configuration can be defined as the configuration of lowest workable threshold.

The counting rate is measured at various mesh voltages (200–400 V) in this configuration of lowest threshold. As showed in Figure 6 (right), it increases with voltage as the charge spectrum shifts above threshold. The trend can be described by an sigmoid function with an inflexion point at 260 V. At this voltage, the rate is per definition half of its maximum value because the threshold is equal to the average pad charge. The smallest detectable charge is thus given by:

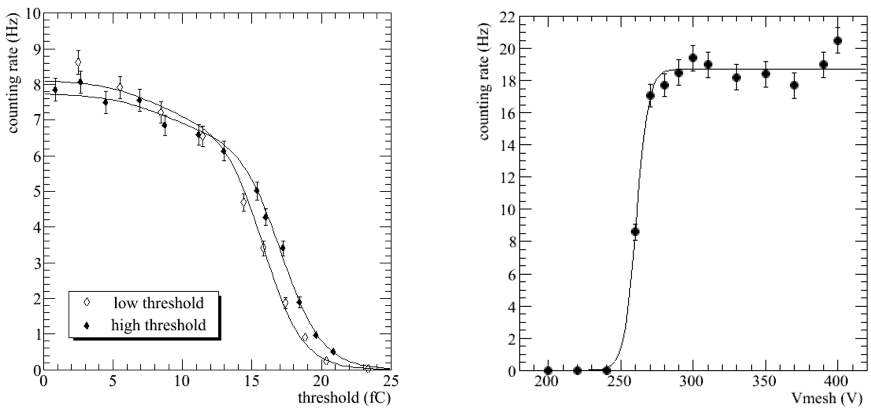

Figure 6. Counting rate versus threshold (left) and mesh voltage (right).

$$Q = q_e\, N\, G = 1.6 \cdot 10^{-4} \cdot 212 \cdot 20 \approx 0.7\,\text{fC} \tag{3.6}$$

where N is averaged over the ^{55}Fe spectrum (*i.e.* $0.85 \cdot 230 + 0.15 \cdot 115$). Previous measurements ([14]) showed that high MIP efficiency (>95 %) is reached when the most probable value of the charge is ~ 3 times larger than the threshold. Taking a most probable number of primary electrons of 14 (ref X), it can be inferred this condition will be met at gas gains of 1000–2000.

3.2.3 Position scan

The uniformity of the gas gain and of the thresholds can be verified by measuring the X-ray counting rate at various positions and for different ASUs. For a given ASU, the position scan is carried out on 6 different positions. At each position the source is collimated onto a region of 2×2 pads centred in between 4 chips (Figure 7 (left). In this way, it is possible to involve all 24 ASU chips in the counting experiment. For this study, all channels are enabled and their thresholds are equalised according to the procedure explained in section X. The mesh voltage is set at 320 V at which an average ^{55}Fe signal of ~ 5 fC is expected. With the given collimation of the source and the transverse electron diffusion in the gas, the count rate has now to be calculated over an 8×8 pad region.

Position scans have been performed for 6 ASU before assembly in the $1 \times 1\,\text{m}^2$ prototype. As illustrated in Figure 7 (right), the response of the channels to the source is uniform. A flat noise-free background from cosmic particles can be seen when plotting the channel occupancy in a logarithmic scale. The results are summarised in Table 1. For each ASU, the spread of the counting rate was observed not to exceed 3 % RMS. Small ASU to ASU variations of the mean rate are observed, probably due to change of atmospheric conditions from one test to the next.

The conclusion of the ASU tests prior assembly inside the $1 \times 1\,\text{m}^2$ prototype is that the manufacturing technique (so-called Bulk) and the calibration procedure allow to achieve very low detection threshold, negligible noise and good response uniformity in a reproducible way. After careful characterisation of 6 ASU, the first $1 \times 1\,\text{m}^2$ Micromegas prototype with MICROROC readout was constructed in May 2011 and subsequently tested in beam in July. The results of the test-beam are presented in the next section.

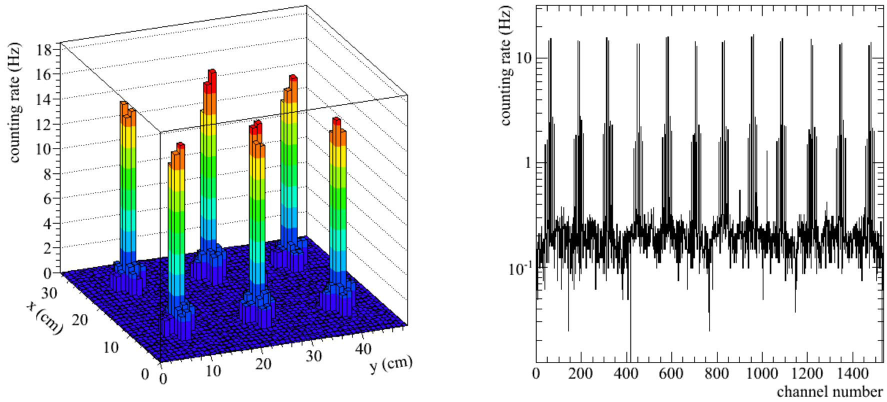

Figure 7. From left to right: two dimensional and one dimensional channel occupancy obtained when moving an ^{55}Fe source over 6 positions.

ASU number	1	2	3	4	5	6
Rate mean (Hz)	86.2	85.2	87.0	79.3	84.2	84.3
Rate RMS (Hz)	2.0	1.7	1.1	1.6	2.2	2.5

Table 1. ^{55}*Fe quanta counting rates measured on 6 ASU (6 measurements per ASU).*

4. Functional tests of the prototype in particle beams

The goal of the test-beam was to validate the mechanical design of the $1 \times 1\,\mathrm{m}^2$ prototype, to measure its response to MIPs and to test its principal functionalities. The test set-up consists of the large prototype and a telescope of small Micromegas chambers and 3 scintillating paddles of $6 \times 16\,\mathrm{cm}^2$ read out by photomultiplier tubes (PMT) (see [14] for a detailed description of the telescope). This setup-up was installed at the CERN SPS facility in the beam line H4 and exposed to 150 GeV/c muons and pions. The position of all Micromegas chambers are such that the beam trajectory is perpendicular to their pad plane. During the pion runs, a 20 cm long block of iron ($10 \times 10\,\mathrm{cm}^2$ cross-section) was placed between the telescope and the prototype to study its behaviour in hadron showers. The trigger was generated by the time coincidence of the 3 PMT signals and delayed by 1.5 μs before reaching the detectors in order to accommodate for the peaking time of the $1 \times 1\,\mathrm{m}^2$ prototype electronics.

4.1 Noise conditions in triggered operation

The noise conditions are evaluated by identifying in the $1 \times 1\,\mathrm{m}^2$ prototype data the contributions from beam muons, cosmics particles and electronic noise. To this end, a low intensity muon beam of 250 Hz collimated to roughly the size of the scintillators ($\sim 100\,\mathrm{cm}^2$) was used. The mesh voltage was set to 370 V at which a MIP efficiency larger than 95 % is reached (cf. section 4.4). The

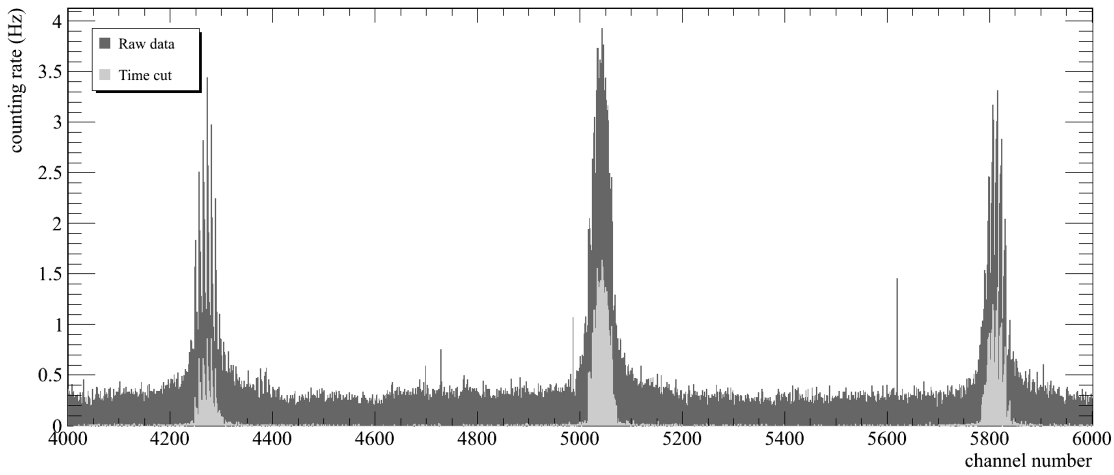

Figure 8. Channel occupancy for all hits and for hits in time with the trigger (right).

thresholds were equalised according to the procedure previously described, resulting in a number of disabled channels of 10.

The three contributions can be seen in Figure 8 which depicts the counting rate of $\sim 25\,\%$ of the prototype channels. Beam muons appear as broads peaks (the peak shapes are partly the result of the channel mapping) and a few relatively noisy channels are spotted as isolated peaks. The background from cosmic particles is essentially flat which demonstrates good noise conditions. By applying a cut on the time of the trigger ($\Delta t = 1\,\mu$s), cosmics and noise hits are fully suppressed as illustrated in Figure 8. It can be noted that this cut removes some hits from beam particles as well. These particles traverse the prototype during a readout. Although vetoed by the trigger, they can still be recorded by the prototype because its dead time is shorter than that of the telescope and because its electronics is self-triggered.

4.2 Trigger-less operation

Thanks to the excellent noise conditions reported in the previous section, the 1×1 m^2 prototype can actually be operated without an external trigger. In this trigger-less mode, no telescope nor trigger electronics are used: the prototype is read out when a memory full signal sent by a MICROROC is received at a DIF board (in trigger mode, a memory full signal resets all chip memory and does not introduce dead time). The beam and voltage settings of the trigger mode test are used.

A simple way to verify that the prototype is efficiency in this mode is to compare the average time between readouts in spill to its expected value. The latter is calculated simply as the ratio of the memory event depth (127) to the highest chip counting rate ($\sim 130\,$Hz) and is roughly 1 s. This is in agreement with measurements as illustrated in Figure 9 (left). Another evidence for an efficient operation of the prototype in trigger-less mode is showed in 9 (right) where the channel counting rates in the two modes are compared and are similar. Successful operation without trigger is possible because of the negligible noise and spark rates which are the result of a precise electronic calibration and a reliable mesh manufacturing technique.

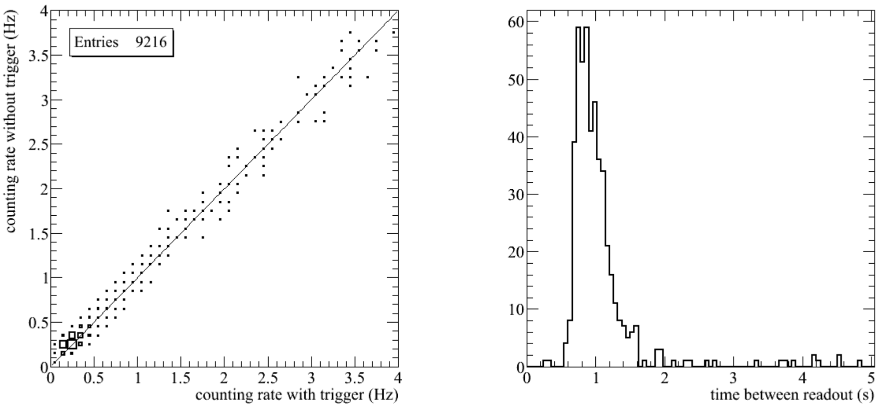

Figure 9. Channel counting rate during spills (left): trigger versus self-trigger mode. Time between readout in trigger-less mode (right).

4.3 Response of the six Micromegas meshes

The prototype was moved across the beam to measure the fake hit probability, efficiency and hit multiplicity of the 6 ASU. A muon beam of similar intensity as in the previous studies was directed at the centre of each ASU. At each position, roughly 100 thousand triggers were recorded. Efficiency and hit multiplicity are deduced from the distribution of the number of hits per triggering muons. This distribution is built by finding a track in the telescope, extrapolating its impact at the prototype and counting the number of hits in time with the trigger inside a search region centred around the pad containing the extrapolated track position. Events are selected by applying the following cuts:

1. Telescope cut
   Single aligned hits in the 3 chambers to select tracks with minimum angle w.r.t. the beam axis and to extrapolate the track position at the prototype in the most precise way. This cut reduces the statistics by roughly one third.

2. Prototype cut
   No hits in time with the trigger outside the search region to reduce the impact of multiple scattering on the measured efficiency. The radial distribution of hits (in time with the trigger) w.r.t. the extrapolated pad falls rapidly and has a long tail from muons scattered in the last telescope chamber. As a result, a search region of 7×7 pads is chosen. This cut reduces further the statistics by 5 %.

About 30 thousand events pass the selection, for each ASU. The distribution of the number of hits above the low threshold is showed in Figure X. The efficiency ε is calculated as the probability to have at least one hit in the search region:

$$\varepsilon = 1 - N_0 / N_\mathrm{t} \tag{4.1}$$

and the hit multiplicity m as the average number of hits in the search region provided there is at least one hit in the search region:

$$m = \sum_{\mathrm{i}=1}^{21} i \, \frac{N_{\mathrm{i}}}{N_{\mathrm{t}} - N_0} \tag{4.2}$$

where N_{i} is the number of events with “i” hits and N_{t} the total number of events. Efficiency and hit multiplicity have been calculated for the 6 ASU and for the 3 thresholds. For the low threshold, high efficiency and low multiplicity are observed, with little spread from ASU to ASU (Table 2). As expected, smaller values are observed for the medium and high thresholds. Because these two thresholds are set within the signal distribution, their response is more sensitive to detector non-uniformity than the one of the low threshold and indeed, more spread is observed. These variations could be due to small difference of the amplification gap size from one ASU to the other. They are, however, not too large and could be attenuated by adjusting the mesh voltage or the corresponding chip thresholds. In section 4.7, a way to calculate these corrections using the direct readout of shaper signals is presented.

ASU number	1	2	3	4	5	6
eff0 (%)	97.9	97.6	98.8	98.4	98.3	96.8
mult0	1.138	1.146	1.154	1.173	1.136	1.148
eff1 (%)	36.4	38.2	47.7	42.9	39.9	47.4
mult1	1.078	1.079	1.088	1.091	1.081	1.083
eff2 (%)	4.1	4.1	5.2	4.6	4.6	5.2
mult2	1.088	1.089	1.097	1.108	1.090	1.078

Table 2. *MIP efficiency and hit multiplicity of the tree thresholds on the 6 ASU of the prototype.*

4.4 Effect of the peaking time

The MICROROC chip was designed for use with various MPGD geometries, for instance with a Bulk mesh of different gap size or even with a Gas Electron Multiplier structure. For this purpose, the peaking time of the preamplifier can be set to 75, 115, 150 or 200 ns (the latter being the default value of the $1 \times 1\,\mathrm{m}^2$ prototype). In the gas mixture used, the signal from the multiplication of a single primary electron in a 128 μm gap consists of a fast electron peak ($\sim$ 1 ns) and a long ion tail ($\sim$ 100–200 ns). For a traversing MIP, the signal is the sum of, on average, 30 primary electrons arriving at the mesh in about 30 ns. Therefore, a strong dependence of the efficiency on the peaking time is expected and should be measured.

This dependence was measured by performing voltage scan for the 4 different values of the peaking time in a muon beam directed at the centre of one ASU. The efficiency is calculated as explained in section X. The 150 ns and 200 ns trends showed in Figure 10 are similar, meaning that

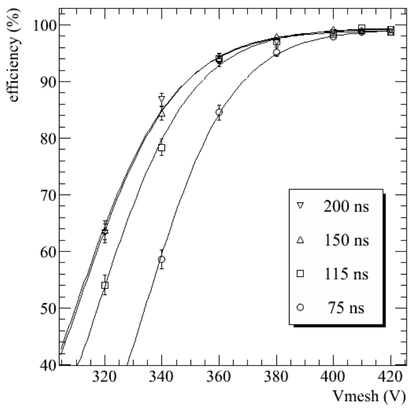

Figure 10. MIP efficiency versus mesh voltage for various peaking time of the MICROROC.

the Micromegas MIP signal is completed in 150 ns or less. The loss of efficiency from 150 ns to 115 ns peaking time indicates, however, that the signal lasts longer than 115 ns which is compatible with expectations. At shorter peaking times, an efficiency larger than 95 % can be maintained by increasing the gas gain. This is illustrated in Table X where the voltages for 95 % efficiency are summarised: the loss of signal when changing the peaking time from 200 ns to 75 ns is compensated by a 20 V increase of mesh voltage. These voltages are calculated using the empirical parametrisation:

$$\varepsilon(V) = \frac{p_0}{1 + \exp\left(\frac{p_1 - V}{p_2}\right)} \tag{4.3}$$

where p_0 is the efficiency at infinite voltage, p_1 is the voltage for 50 % efficiency and p_2 describes the rise of the $\varepsilon(V)$ trend. All adjusted p_0 parameters are compatible and yield an average of 99.3 ± 0.3 %. The fact that the asymptotic value is not equal to 1 could be explained by the dead zone of the mesh supporting pillars. The voltage p_1 decreases at longer peaking time as a result of the increased available signal and becomes constant between 115–150 ns. At decreasing peaking times below 115 ns, the efficiency rises faster with voltages which is accounted for by smaller p_2 values.

4.5 Impact of dead zones between ASUs

Non-instrumented areas inside the prototype amount to 1.5 % of the total area occupied by the 6 ASUs ($96.5 \times 97\,\mathrm{cm}^2$). Another contribution to the prototype inefficiency may come from possible non-uniformity of the electric field at the ASU edges. This hypothesis was tested by placing a block of iron along a pion beam (collimated to a $3 \times 3\,\mathrm{cm}^2$ region) and measuring downstream of the block secondary particles produced in hadron showers. In this way a large fraction of the prototype is exposed and possible discontinuities in the measured hit profile can be looked for. For this measurement, the mesh voltages were set to 375 V.

Considering the block size ($10 \times 10\,\mathrm{cm}^2$ transverse size and 20 cm length along the beam), roughly half of the pions experience a nuclear interaction inside the block. The distribution of the

t_{p} (ns)	75	115	150	200
p_0 (%)	99.3 ± 0.3	99.6 ± 0.3	99.4 ± 0.3	99.1 ± 0.3
p_1 (V)	333.9 ± 0.7	317.4 ± 0.8	310.1 ± 0.9	309.4 ± 0.8
p_2 (V)	15.2 ± 0.5	16.3 ± 0.7	17.0 ± 0.8	17.1 ± 0.7
$V(\varepsilon = 95\,\%)$ (V)	380.9	366.7	362.6	363.0

Table 3. *Parameters describing the voltage dependence of the efficiency fot various peaking time of the MICROROC. The voltage necessary to reach an efficiency of 95 % is indicated in the last line*

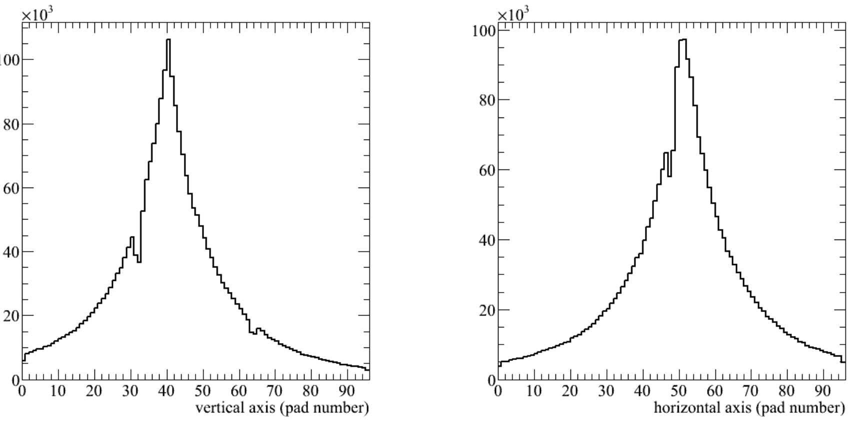

Figure 11. Vertical and horizontal profiles of pion showers (~ 50 thousand events).

number of hits in the prototype thus shows a peak at $N_{\mathrm{t}} = 1$ from penetrating pions and a long tail up to $N_{\mathrm{t}} = 300$ from showering pions (Figure X). Horizontal and vertical profiles of showers only are constructed by rejecting events with a hit multiplicity below 3. They are showed in Figure 11 where a clear drop of efficiency for pads at the ASU edge is observed. By extrapolation of the inner pad occupancy to the ASU edges, the number of hits is 20 % lower than what it should be. The number of pads at the ASU edges is 576 (out of 9216 which yields a fraction of 6.2 %). This can be interpreted as a dead zone of 1.25 % which adds to the 1.5 % from non-instrumented areas, leading to less than 3 % of the prototype being inefficient.

4.6 Shower sampling with three readout thresholds

Hadron showers develop on average in a dense electromagnetic core from neutral meson decays surrounded by a halo of particles (muons, charged pions, protons etc...). Saturation in a DHCAL will be caused mainly by the electromagnetic part and additional thresholds are introduced to perhaps mitigate this effect by identification and weighting of low, medium and high energy deposits. This identification capability can be illustrated by measuring the threshold efficiencies for various energy deposits. Because the energy density decreases with the distance to the shower axis, the

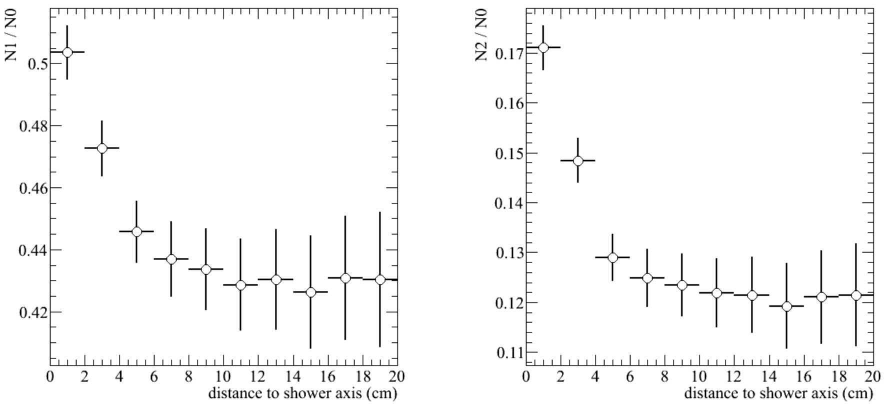

Figure 12. Medium and high threshold efficiency in hadron showers versus distance to the shower axis.

efficiencies were measured as a function of position using the setup-up described in the previous section. The mesh voltage was 370 V and the thresholds were set at (2 fC, 1 MIP, 3 MIP).

Because the MIP efficiency of the low threshold is high ($\leq 95\,\%$), the efficiency of the other thresholds can be approximated to N_1 / N_0 and N_2 / N_0 where N_k is the number of hits from threshold "k". These ratios are plotted versus distance to the shower axis in Figure 12. Both trends indicate that the electromagnetic core is contained in a circle of 10 cm radius. Compared to the halo, the core has a higher energy density which explains the probability variation with distance: $p_{\mathrm{thr}\,1}$ increases from 0.43 to 0.51 and $p_{\mathrm{thr}\,2}$ from 0.12 to 0.17. This measurement illustrates the possibility to identify the electromagnetic part of hadron showers which is a necessary condition for offline compensation of a Micromegas semi-digital hadron calorimeter.

4.7 Analogue readout of shaper signals

Correction of the mesh voltage or the readout threshold may be necessary to improve the response uniformity of the prototype, in particular for the medium and high thresholds (cf. section X). The most straight-forward way to calculate the correction is to have access directly to the signal distribution. For this reason, dedicated lines were implemented on the ASU to read out the output voltage of the low gain shaper. The analogue readout uses a trigger signal that first arrives at the DIF. After a certain programmable delay to match the peaking time of the MICROROC, the DIF forwards the signal at the chips. The voltages of the shaper outputs of all channels are then multiplexed and sent to the DIF where they are digitised with a 12-bit resolution.

The analogue readout was tested in a beam of muons. The Landau distribution as measured on roughly 100 pads and corrected for channel to channel pedestal variations is shown in Figure 13 (left). By applying cuts on low, medium or high thresholds, the signal distribution is cropped from 0 to the threshold value which can thus be measured in unit of charge (Figure 13 (left to right)). More importantly, it is also possible to measure the thresholds in unit of the MIP value which is the natural energy unit in a calorimeter. For instance, threshold and MIP values can be extracted from the data using the following parametrisation of the charge spectrum:

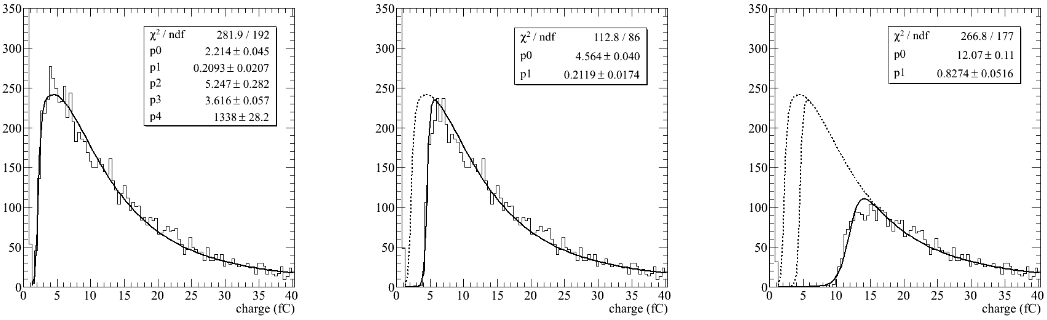

Figure 13. Muon Landau distribution from hits passing low, medium and high thresholds.

$$f(q) = s(q, p_0, p_1) \cdot l(q, p_2, p_3, p_4) \tag{4.4}$$

where $s(q)$ is a sigmoid function of inflexion point p_0, width p_1 and with a maximum value of 1 that accounts for the channel to channel threshold dispersion. The function $l(q)$ is the Landau function of most probable value p_3, width p_4 and normalisation factor p_2. When adjusting the parameters to the data of Figure 13, it is found that low, medium and high thresholds are respectively equal to 0.6, 1.3 and 3.3 times the MIP value.

4.8 Power-pulsing of the front-end chips

The circuits of a MICROROC chip can be turned on and off rapidly according to an external digital signal synchronous to the accelerator clock. When the chip is turned on, a certain programmable delay is applied before any detector signal can be recorded to the memory. This delay accounts for the stabilisation of the various voltages and currents inside the chip and should be minimum to reduce the power consumption. If the delay is too short, the detector occupancy is dominated by noise until stabilisation. This is illustrated in Figure 14 (left) where the number of hits in the $1 \times 1\,\mathrm{m}^2$ prototype is plotted versus time for a short run in trigger-less mode. During the run, a power-pulsing timing of 4.5 s off and 3 s on was used and the delay was set to $50\,\mu$s. When using a delay of $100\,\mu$s (Figure 14 (right)), the high peaks every 7.5 s disappear because stabilisation has been achieved. For a bias voltage of 5 V, the current drops from 11 A to 3 A when the chips are turned off. The 3 A correspond to the consumption of the 3 DIF and inter-DIF boards of the prototype.

5. Conclusion

A Micromegas prototype of $1 \times 1\,\mathrm{m}^2$ consisting of six independent Micromegas boards with integrated 2-bit front-end electronics has been constructed. This modular design, although introducing little dead zones (below 3 %), allows to achieve an overall thickness of 9 mm and a uniform drift gap over the prototype area. Thanks to adequate discharge protections and low noise front-end circuits, more than 99.98 % of the 9216 prototype channels are operational. Most importantly, the six Micromegas boards exhibit comparable performance to ionising radiations and all provide the necessary gas gain for a 98 % efficiency to minimum ionising particles.

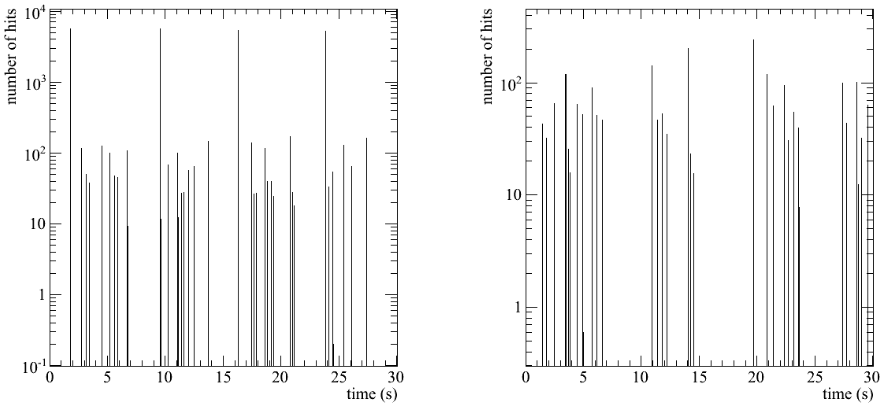

Figure 14. Number of hits versus time using power-pulsing of the chips with 50 μs (left) and 100 μs (right) delay between the power signal and the start of the trigger-less acquisition.

Compared to a pure digital gaseous calorimetry, an approach with three threshold will probably rely strongly on the proportionality of the sampling detector and on its cell to cell signal uniformity. This kind of Micromegas is free of saturation effects and its amplification gap is precisely defined by the mesh supporting pillars over the anode plane. Variations of this gap have probably been observed from mesh to mesh. Based on the direct readout of detector signals, however, a technique to correct the mesh voltage of chip thresholds is possible. Combined with other features such as power-pulsing and self-triggering, the constructed Micromegas prototype is therefore a good candidate for Particle Flow hadron calorimeter at a future linear collider.

Acknowledgments

Acknowledgments.

References

[1] Authors, *Title*, *J. Ref.* **vol** (year) page.

[2] Authors, *Title*, *J. Ref.* **vol** (year) page.

[3] Authors, *Title*, *J. Ref.* **vol** (year) page.

[4] Authors, *Title*, *J. Ref.* **vol** (year) page.

[5] Authors, *Title*, *J. Ref.* **vol** (year) page.

[6] Authors, *Title*, *J. Ref.* **vol** (year) page.

[7] Authors, *Title*, *J. Ref.* **vol** (year) page.

[8] Authors, *Title*, *J. Ref.* **vol** (year) page.

[9] Authors, *Title*, *J. Ref.* **vol** (year) page.

[10] Authors, *Title*, *J. Ref.* **vol** (year) page.

[11] Authors, *Title*, *J. Ref.* **vol** (year) page.

[12] Authors, *Title*, *J. Ref.* **vol** (year) page.

[13] Authors, *Title*, *J. Ref.* **vol** (year) page.

[14] Authors, *Title*, *J. Ref.* **vol** (year) page.

[15] Authors, *Title*, *J. Ref.* **vol** (year) page.

[16] Authors, *Title*, *J. Ref.* **vol** (year) page.

[17] Authors, *Title*, *J. Ref.* **vol** (year) page.

[18] Authors, *Title*, *J. Ref.* **vol** (year) page.

[19] Authors, *Title*, *J. Ref.* **vol** (year) page.

[20] Authors, *Title*, *J. Ref.* **vol** (year) page.

[21] Authors, *Title*, *J. Ref.* **vol** (year) page.

[22] Authors, *Title*, *J. Ref.* **vol** (year) page.

[23] A. Pietropaolo et al., *DINS measurements on VESUVIO in the resonance detector configuration: proton mean kinetic energy in water*, 2006 *JINST* **1** P04001.

[24] A.I. Harris, *Spectroscopy with multichannel correlation radiometers*, *Rev. Sci. Instrum.* **76** (2005) 054503 [astro-ph/0504449].

[25] G.F. Knoll, *Radiation detection and measurements*, John Wiley and Sons, Inc., New York 2000.

[26] V. Dangendorf, *Time-resolved fast-neutron imaging with a pulse-counting image intensifier*, in proceedings of *International workshop on fast neutron detectors and applications*, April, 3–6, 2006 University of Cape Town, South Africa PoS(FNDA2006)008.